Investigation of gas diffusion media inside PEMFC using CFD modeling

S. Shimpalee [a,*], U. Beuscher [b], J.W. Van Zee [a]

[a] *Department of Chemical Engineering, University of South Carolina, Columbia, SC 29208, United States*
[b] *W.L. Gore & Associates, Inc., 201 Airport Road, Elkton, MD 21922-1488, United States*

Abstract

The performance of a gas diffusion layer comprised of a macro porous and micro porous layer has been studied both experimentally and by numerical simulation. Experimental data at different humidification conditions have been compared to full cell, three-dimensional computational fluid dynamics calculations to validate the physical model of the cell. Local distributions of current density, electrochemical variables, temperature, and gas composition are discussed in detail. Model calculations agree well with experimental data and the solutions with and without the micro porous layer show that this layer has an effect on the overall performance and the local distributions show differences. The effect of hydrogen dilution is also explored in this paper with micro/macro gas diffusion media. The results reveal that proton exchange membrane fuel cell (PEMFC) performance depends not only on the oxygen but also on the hydrogen partial pressure.
© 2006 Elsevier B.V. All rights reserved.

1. Introduction

Proton exchange membrane fuel cells (PEMFCs) use gas diffusion layers (GDLs) to enhance the reaction area accessible by the reactants. The effect of using these GDLs is to allow a spatial distribution in the current density on the membrane electrode assembly (MEA) in both the direction of the flow and parallel to the MEA. In addition, the GDL has to ensure proper transport of product water, electrons, and heat of the reaction. Porous carbon materials are most often used to accomplish this complex task. A micro porous layer or diffusion layer [1,2] is sometimes added between the main macro porous GDL and the membrane electrode assembly as illustrated in Fig. 1. The purpose of this micro layer is to aid in the distribution of the reacting gas flows to the MEA surface, the mechanical compatibility between the layers, the contact resistance, local current density distribution, and water management. The micro layer is usually comprised of carbon for electrical conductivity and PTFE for hydrophobicity. The objective of this study is to understand the role of the micro porous layer as well as the interactions with the macro layer and the flow-field configuration.

Computational fluid dynamics (CFD) is gaining more interest as a tool to understand fuel cell performance as reviewed by Wang [3] and Baschuk and Li [4]. Many research groups [5–17] are improving their computational models to be more realistic, faster in computing, or to be able to be used for design improvement. For example, Meng and Wang [8] improved their three-dimensional (3D) CFD model to be more realistic so that it can investigate two-phase behavior under different gas utilizations even though the energy transport was ignored. Kulikovsky et al. [10] demonstrated a simplified analytical model to obtain physical parameters and then input those parameters into a quasi-3D model to speed up the PEMFC calculation. Oosthuizen et al. [13] used a 3D model to study the gas crossover between side-by-side channels under different flow rates, channel path length flow fields, and GDL porosities. Their results might be useful for flow-field design improvements of the PEMFC. The multidimensional model calculations provide insight into the fuel cell on a local level and describe distributions of current, heat, and water. Thus, modeling will help in gaining an understanding of the mechanisms inside the fuel cell, aid in experimental data analysis, and identify limiting parameters. In this study, exper-

---

* Corresponding author. Tel.: +1 803 576 6140; fax: +1 803 777 8265.
E-mail address: shimpale@engr.sc.edu (S. Shimpalee).

Nomenclature

F	Faraday constant (96,487 C mole of electrons^{-1})
i	local current density (A m^{-2})
i_0	exchange current density (A m^{-2})
P	pressure (Pa)
R	universal gas constant (8.314 J mol^{-1} K^{-1})
T	temperature (K)

Greek symbols

η	overpotential for oxygen reaction (V)

Subscripts

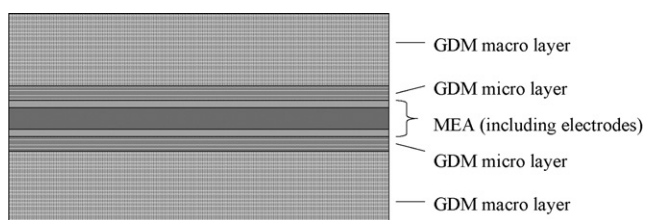|	
H_2	hydrogen
in	inlet
O_2	oxygen

Fig. 1. Schematic representation of GDM layers and the MEA.

imental performance data are compared to numerical results to validate the CFD model and to investigate the local distributions. The effect of dilution of hydrogen in nitrogen on the anode side has also been studied numerically. Furthermore, the effect of the micro porous layer is analyzed by comparison of numerical results to calculations without the micro layer.

2. Experimental

Experimental data were obtained with 40% hydrogen in nitrogen on the anode and air on the cathode using a 5620 PRIMEA®[1] membrane electrode assembly from W.L. Gore & Associates, Inc. (Elkton, MD). It was assembled in a 25-cm^2 test cell (Fuel Cell Technologies, Inc., Albuquerque, NM) using SGL hydrophobized macro gas diffusion media (SGL Carbon AG, Meitingen, Germany) and CARBEL® MP micro gas diffusion media (from W.L. Gore & Associates, Inc.). The average compression in the cell was about 150 psi. The cell contained a triple serpentine flow pattern and was operated in the co-flow configuration. All tests were performed with a standard gas delivery unit (Globe Tech, Inc., Bryan, TX) with a Scribner 890b electronic load with PC control (Scribner Associates, Inc., Southern Pines, NC). All mass flow controllers and sparger bottles were calibrated for flow rate and dew point, respectively. All polarization curve data were collected using automated test protocols

---

[1] PRIMEA, CARBEL and GORE and designs are trademarks of W. L. Gore & Associates, Inc.

(Fuel Cell^{TM} software by Scribner Associates, Inc.) by holding 10 min at each set point and averaging the last minute of collected data. The operating conditions were 65 °C cell temperature with 0 psig back pressure and an anode and cathode stoichiometry of 1.2 for H_2 on 40% H_2/60% N_2 and 2.0 for air, respectively. The gas humidification was varied during the experiments for a robust validation of the model calculations compared to the experimental data over a range of operating conditions. Four conditions were tested focusing on inlet humidity conditions: fully humidified gas streams (condition #1: 65 °C/65 °C dew point on anode and cathode, respectively), highly oversaturated streams (condition #2: 85 °C/85 °C), dry anode (condition #3: dry/65 °C), and dry cathode (condition #4: 65 °C/dry).

3. Numerical

This numerical simulation is based on a three-dimensional computational fluid dynamics model of a full-cell PEM fuel cell with temperature dependence and water phase change. The actual flow path geometry was taken from the single experimental laboratory cell and consists of a triple serpentine gas channel that has 10 passes as shown in Fig. 2. A thin membrane electrode assembly is sandwiched between anode and cathode diffusion layers that have a micro structure on the surface of the MEA. The MEA consists of a membrane and two electrodes comprised of dispersed carbon supported platinum catalysts. Fig. 3 shows the geometrical details, which consists of the anode flow channel, anode diffusion layer, MEA, cathode diffusion layer, and cathode flow channel. The flow channel has dimensions of 0.09 cm (height) × 0.07 cm (width) cm cross-section flow area in each channel with the length of 5.00 cm. Each diffusion layer (macro and micro) has dimensions of 0.033 cm (height) × 5.00 cm (width) × 5.00 cm (length) as shown in the *zoom-in* part of this figure. Therefore, the active area of the MEA is 25 cm^2. A total of 929,040 cells (elements) were used in the flow channels and gas diffusion layers to model the fuel cell.

3.1. Model equations

The equations solved in this work included the conservation of mass, the Navier–Stokes equations, the species transport equations, the energy equation, and a water phase change model, where homogeneous two-phase flow was assumed. In the water phase change model, when the local activity of water exceeded 1.0, water vapor was condensed to form liquid water until the local activity equaled 1.0. Conversely, if liquid water was present and the local activity of water dropped below 1.0, then liquid water was evaporated until the local activity equaled 1.0. When liquid water condensed in the region adjacent to the electrode surface, it is assumed to form a liquid film on the electrode surface. In the regions where there was a liquid film on the electrode, hydrogen and oxygen were required to dissolve in the liquid film and diffuse through the film to the electrode surface in order to react. Henry's law was used to calculate the solubility of the gases in the liquid. The thickness of this liquid film depends on the rate of condensation/evaporation and the production of water
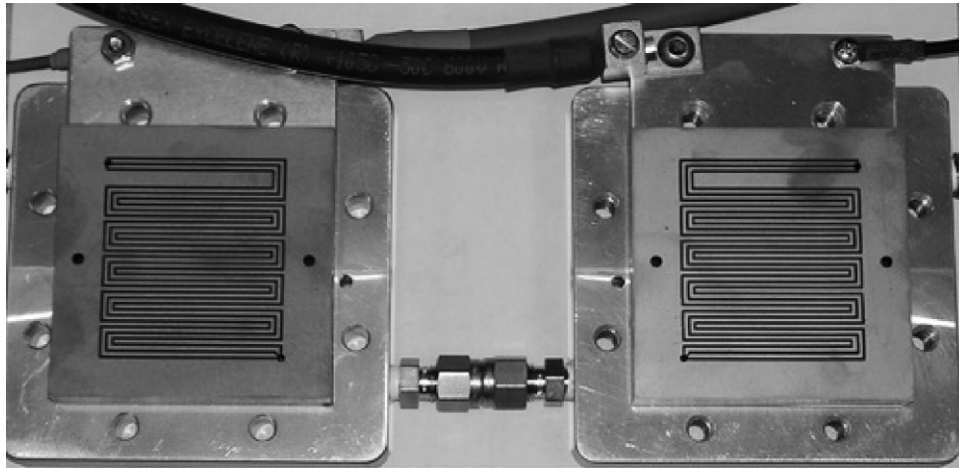
Fig. 2. The picture shows actual flow-field plate with the gas channel. There are 10 straight channels connected in a triple serpentine fashion. Anode side and cathode side flow channels are symmetric and placed properly aligned (non-staggered) on top of each other.

by electrochemical reaction as discussed in the appendix of Lee et al. [5].

A control volume technique based on a commercial flow solver, STAR-CD 3.26, was used to solve the coupled governing equations [18]. This software was used with an add-on tool called Expert System for PEMFCs (ES-PEMFC Version 2.20) that provided the source terms for the species transport equations, the phase change equations for water, and the heat generation equations [19]. Also, ES-PEMFC accounted for the flux of protons and water across the membrane [19]. Further, the effect of concentration for both anode and cathode on overpotential has been taken into account as shown in Eq. (1).

$$\eta(x, y) = \frac{RT}{4F} \ln\left(\frac{P_{O_2,in}}{P_{O_2}(x, y)}\right) - \frac{RT}{2F} \ln\left(\frac{P_{H_2}(x, y)}{P_{H_2,in}}\right)$$
$$+ \frac{RT}{0.84F} \ln\left(\frac{i(x, y)P_{O_2,in}}{i_{0,O_2}P_{O_2}(x, y)}\right)$$
$$+ \frac{RT}{2F}\left(\frac{i(x, y)P_{H_2,in}}{i_{0,H_2}P_{H_2}(x, y)}\right) \tag{1}$$

All material properties were determined from ex situ observations except the exchange current density for the hydrogen oxidation reaction, i_{0,H_2}, which was adjusted to obtain a better fit to the experimental data. Those properties used in the model are given in Table 1. The results will be presented in the form of distributions of current density, membrane conductivity, temperature, liquid water fraction, and alpha. The net water transfer coefficient per proton, alpha, is a measure of the water management in the cell. A positive value indicates that electro-osmotic drag dominates over back diffusion and a net transport of water from anode to cathode. A negative value for alpha shows a net transport from cathode to anode. A well-balanced fuel cell will result in an alpha value close to zero [5].

4. Results and discussion

4.1. Model validation

Fig. 4 shows four polarization curves taken from experimental data compared to six numerical solutions. A cell potential
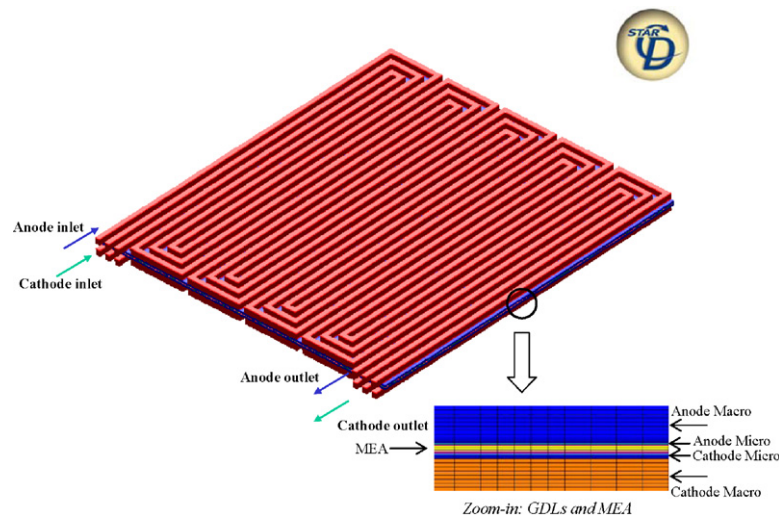

Fig. 3. The geometrical model of the 25-cm² triple serpentine flow-field.

Table 1
GDL properties and MEA properties

| Macro GDL	
Thickness after compressed (μm)	270
Permeability (m^2)	1.0e−09
Porosity after compressed (%)	80
Diffusion adjustment (%)	40
Thermal conductivity (W m^{-1} K^{-1})	0.3
Micro GDL	
Thickness after compressed (μm)	60
Permeability (m^2)	2.1e−13
Porosity after compressed (%)	50
Diffusion adjustment (%)	10
Thermal conductivity (W m^{-1} K^{-1})	0.3
Membrane electrode assembly	
Thickness (μm) (including 12.5 μm thickness of catalyst layer)	50
Thermal conductivity (W m^{-1} K^{-1})	0.147
Dry membrane density (g cm^{-3})	2.0
Equivalent weight of dry membrane (g mol^{-1})	1100
Cathode exchange current density (A cm^{-2})	0.0006
Cathode transfer coefficient	0.84
Anode exchange current density (A cm^{-2})	0.6
Anode transfer coefficient	2.0
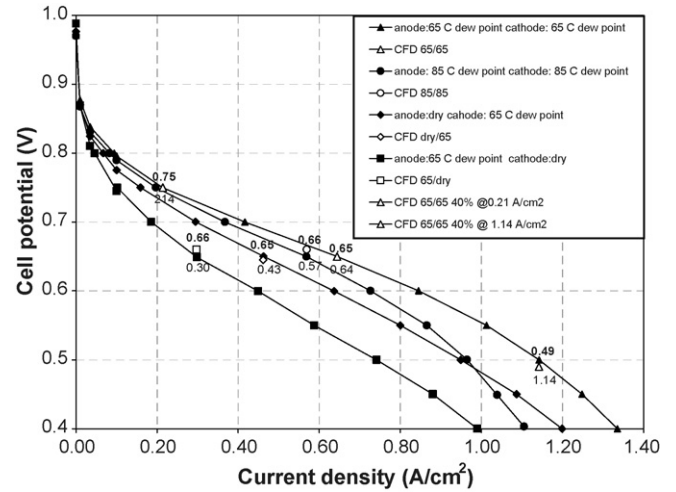
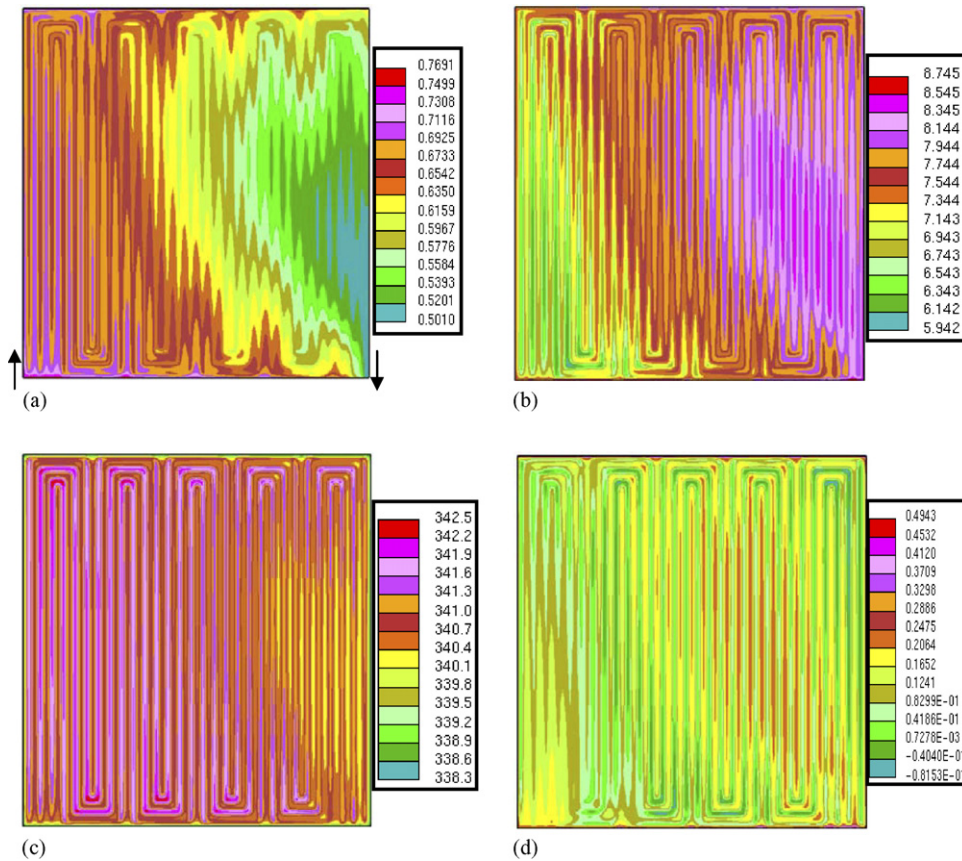Fig. 4. Polarization curves of four operating conditions compared to six calculated points.

Fig. 5. Local distributions on MEA surface at 0.65 V for condition #1: 65 °C anode and 65 °C cathode dew point. (a) Current density distribution (A cm^{-2}), $I_{avg} = 0.64$ A cm^{-2}. (b) Membrane conductivity distribution (S m^{-1}), $\sigma_{avg} = 7.7$ S m^{-1}. (c) Temperature distribution (K), $T_{avg} = 341.2$ K. (d) Alpha distribution, $\alpha_{avg} = 0.083$.

of about 0.65 V at four different humidification conditions was chosen to compare to the model calculations and two more data points were calculated at current densities of 0.21 A cm^{-2} and 1.14 A cm^{-2} of condition #1. The numerical results agree very well with experimental data for all cases. Both experiment and numerical calculations show that condition #1 (65 °C anode dew point and 65 °C cathode dew point) gives the highest performance with a current density of 0.64 A cm^{-2} and condition #4 (65 °C anode dew point and dry cathode) gives the lowest performance with a current density of 0.30 A cm^{-2}. Further, condition #2 (85 °C anode dew point and 85 °C cathode dew point) gives lower performance (0.57 A cm^{-2}) than condition #1 due the partial flooding of the MEA. Finally, condition #3 (dry anode and 65 °C cathode dew point) provides a current density of 0.46 A cm^{-2} at 0.65 V. In addition, model simulations for condition #1 at current densities of 0.21 A cm^{-2} and 1.14 A cm^{-2}, which are in the kinetic and mass transfer limited regions, respectively, also compare very well to experimental data.

Fig. 5 presents the local current density, membrane conductivity, temperature, and alpha distributions on the membrane surface for condition #1 (65 °C/65 °C dew point). Fig. 5a shows the current density distribution with an average of 0.64 A cm^{-2} at 0.650 V. The distribution is very non-uniform with the highest current density of 0.77 A cm^{-2} at the entrance region toward

the outlet with the lowest value of about 0.50 A cm^{-2}. This is caused by the concentration reduction of the reacting gases even though the membrane conductivity increases from inlet toward outlet as shown in Fig. 5b. The membrane conductivity increases from inlet to outlet due to an increase in water activity. Even though the gases enter the fuel cell fully humidified, the water vapor activity inside the cell is less than unity due to the increased temperature of up to 70 °C caused by the heat of reaction. Further, the current density is slightly lower at the inner channel of the triple serpentine compared to the outer channel in the region of the channel bends. This is because the velocity magnitude is lower at the inner bend than the outer bend. Therefore, the heat transfer coefficient of the inner bend is lower than at the outer bend. Thus, the temperature of the inner bend is higher than the outer area as shown in Fig. 5c and this creates the lower membrane conductivity at the inner bend than outer bend shown in Fig. 5b. The distribution of the net water transfer coefficient alpha as shown in Fig. 5d is very uniform and has an average value close to zero (i.e., 0.08) indicating a good balance of water transport between anode and cathode.

Fig. 6 presents the local current density, membrane conductivity, temperature, and liquid water distributions on the membrane surface for condition #2 (85 °C/85 °C dew point). Fig. 6a shows the current density distribution with an average
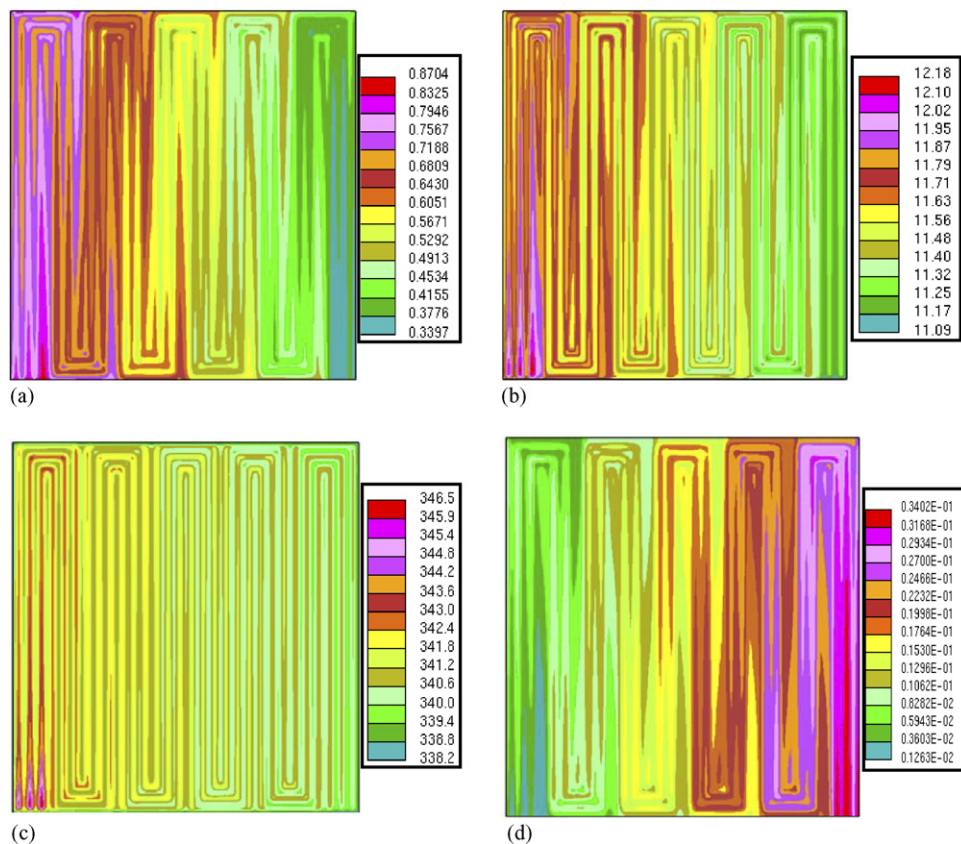

Fig. 6. Local distributions on MEA surface at 0.66 V for condition #2: 85 °C anode and 85 °C cathode dew point. (a) Current density distribution (A cm^{-2}), $I_{avg} = 0.57$ A cm^{-2}. (b) Membrane conductivity distribution (S m^{-1}), $\sigma_{avg} = 11.5$ S m^{-1}. (c) Temperature distribution (K), $T_{avg} = 342$ K. (d) Liquid water mass fraction, average = 0.02.

of 0.57 A cm^{-2} at 0.66 V. The current distribution shows more non-uniformity than the distribution of 65 °C/65 °C dew point. The highest value is 0.87 A cm^{-2} at the entrance region and the lowest value is 0.34 A cm^{-2} at the exit region. The higher inlet humidity applied in this condition leads to a well-hydrated membrane even in the entrance region. Fig. 6b shows that the membrane conductivity is very uniform with a high value. This is because the inlet dew point of both anode and cathode are higher than the actual cell temperature. The cell temperature is high in the inlet region (74 °C) as Fig. 6c shows caused by the high current density and water condensation. However, the temperature drops toward the outlet, which results in the accumulation of liquid water resulting in flooding. Fig. 6d shows that the liquid water fraction increases close to 5% toward the outlet. This significantly affects the concentration of oxygen at the MEA by the liquid water film resistance resulting in a low current density.

Fig. 7 presents the local current density, membrane conductivity, kinetic overpotential, and alpha distributions on the membrane surface for condition #3 (dry/65 °C dew point). Fig. 7a shows the current density distribution with an average of 0.46 A cm^{-2} at 0.65 V. This condition results in the opposite distribution compared with Figs. 5a and 6a. The lowest current density is shown at the entrance region with the value of 0.33 A cm^{-2} and the current density increases toward about 2/3 of the MEA

surface with the value of 0.58 A cm^{-2} then it decreases on the way to the exit to the value of around 0.30 A cm^{-2}. The dry anode inlet results in low membrane hydration at the entrance region, giving the lowest local performance. Further down the cell, water from the cathode humidity and electrochemical reaction is transported across the membrane by back diffusion to hydrate the MEA. This results in increasing membrane conductivity from inlet toward outlet as shown in Fig. 7b. However, the performance decreases from about 2/3 from the cell inlet toward the outlet due to the increasing of kinetic overpotential as shown in Fig. 7c. This figure shows that reacting gases from both anode and cathode are consumed from inlet toward the outlet causing the increasing in overpotential of both surface and concentration with the highest value of 0.30 V. The distribution of alpha in Fig. 7d shows a large negative value in the inlet region, indicating a strong water back transport from cathode to anode. A value less than −0.5 indicates that water from the cathode gas channel in addition to the product water diffuses toward the anode. Toward the outlet of the cell alpha approaches zero, which shows a balance between electro-osmotic drag and back diffusion.

Fig. 8 presents the local current density, membrane conductivity, temperature, and alpha distributions on the membrane surface for condition #4 (65 °C/dry dew point). Fig. 8a shows the current density distribution with an average of 0.30 A cm^{-2} at
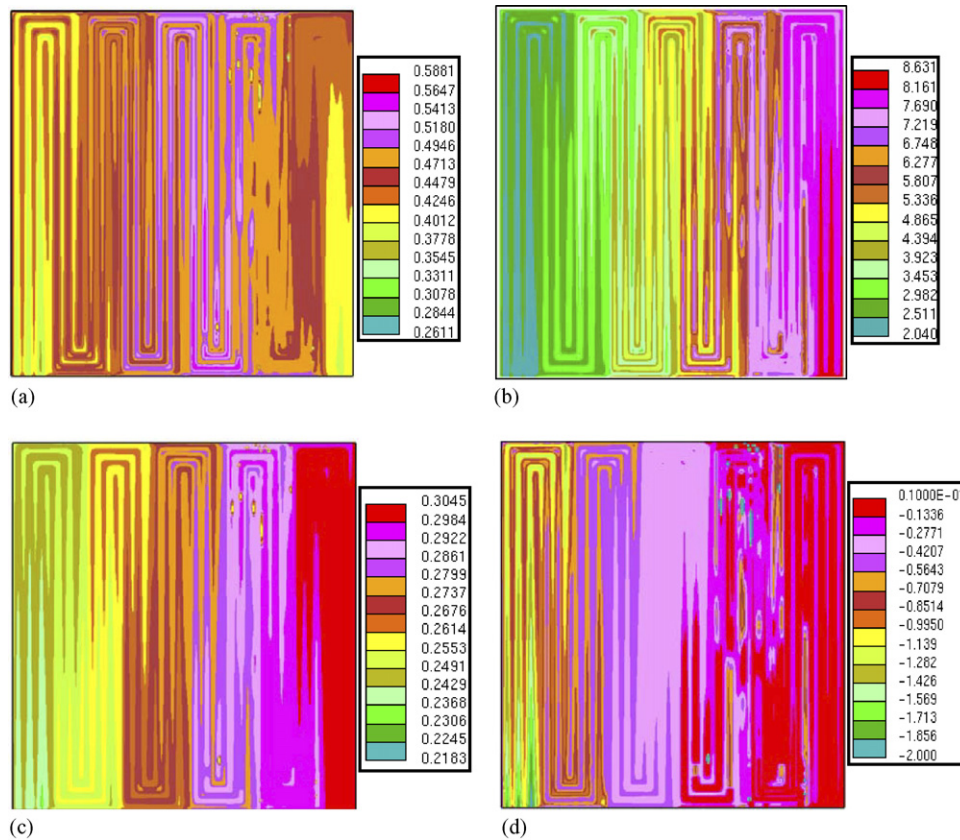

Fig. 7. Local distributions on MEA surface at 0.64 V for condition #3: dry anode and 65 °C cathode dew point. (a) Current density distribution (A cm^{-2}), $I_{avg} = 0.46$ A cm^{-2}. (b) Membrane conductivity distribution (S m^{-1}), $\sigma_{avg} = 5.0$ S m^{-1}. (c) Kinetic over potential distribution (V), $\eta_{avg} = 0.27$ V. (d) Alpha distribution, $\alpha_{avg} = -0.46$.
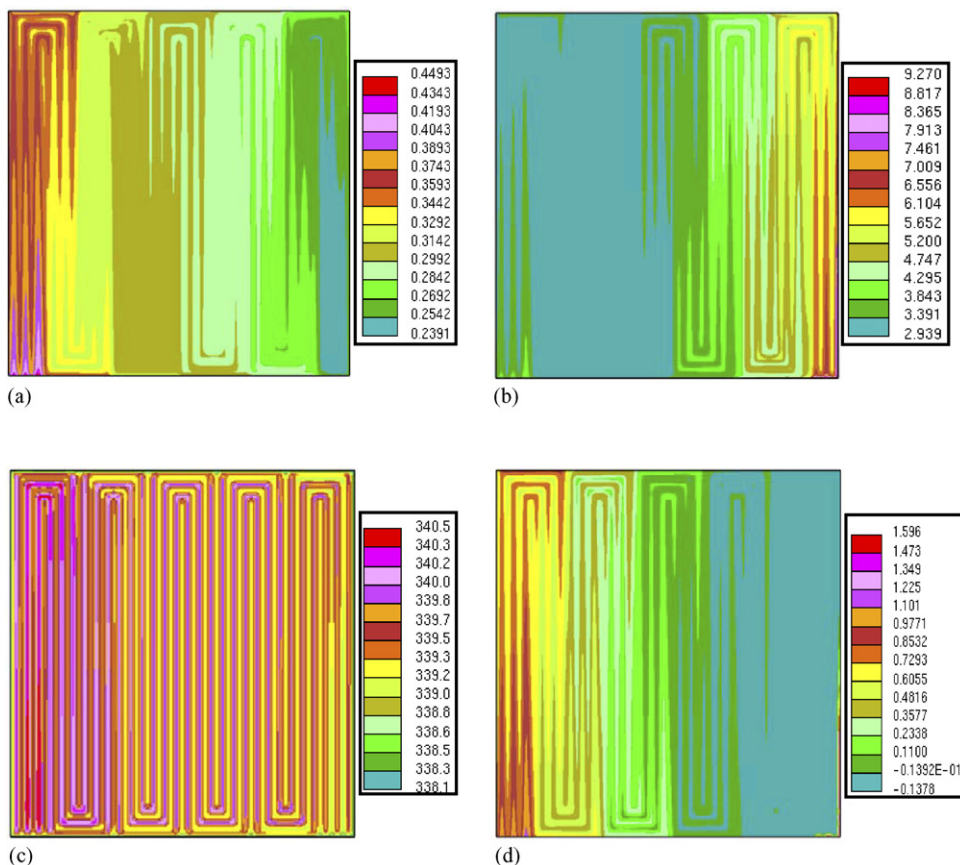
Fig. 8. Local distributions on MEA surface at 0.66 V for condition #4: 65 °C anode dew point and dry cathode. (a) Current density distribution (A cm^{-2}), $I_{avg} = 0.30$ A cm^{-2}. (b) Membrane conductivity (S m^{-1}) distribution, $\sigma_{avg} = 3.8$ S m^{-1}. (c) Temperature distribution (K), $T_{avg} = 340$ K. (d) Alpha distribution, $\alpha_{avg} = 0.22$.

0.66 V. The distribution is similar to Figs. 5a and 6a but the value is much lower. The current density shows the highest value at the inlet region with a value of 0.45 A cm^{-2}. The current density decreases toward the outlet with the lowest value of 0.24 A cm^{-2}. The performance is dominated by the low membrane conductivity illustrated in Fig. 8b, which gives a similar distribution as the current density contour. The low membrane conductivity is due to the reduction of anode water activity by electro-osmotic drag from anode to cathode. The distribution of alpha shown in Fig. 8d indicates that alpha is always positive, which suggests that the electro-osmotic drag dominates over back diffusion even though the current density is low. There is little water back diffusion because of the dry gas on the cathode. The temperature distribution shown in Fig. 8c is very uniform with an average value of 67 °C.

4.2. Effect of cell potential

As stated earlier, the model has also been validated at two data points at condition #1 with a lower and higher cell potential as shown in Fig. 4. In this validation, the flow rate in the model calculation was set according to a low current density of 0.21 A cm^{-2} and a high current density of 1.14 A cm^{-2}. At 0.21 A cm^{-2}, the numerically calculated cell potential is

0.75 V, which exactly matches the experimental value and at 1.14 A cm^{-2} the calculated potential is 0.49 V compared to the experimental value of 0.50 V. These calculations were performed with the same input parameters as before indicating that the model can predict the entire polarization curve and represents both kinetic and mass transport effects very well.

The distributions of current density for these two data points are shown in Fig. 9. The results reveal that the uniformity of the distribution depends on cell potential or amount of electrochemical reaction. With higher reaction rate, i.e., higher current density, the distribution is more non-uniform (max: 1.56 A cm^{-2}, min: 0.65 A cm^{-2}) than at lower reaction (max: 0.25 A cm^{-2}, min: 0.15 A cm^{-2}) and this phenomenon does not appear to be dependent on the GDL characteristics.

4.3. Hydrogen dilution effects

The effect of hydrogen dilution on PEMFC performance was also studied in this work. All previous numerical results and experimental data were performed for 40% H$_2$ and 60% N$_2$ as the anode gas stream. In this part of the study, model calculations were performed for the case of humidification condition #1 at an average current density of $I_{avg} = 0.64$ A cm^{-2} with a composition of the anode gas stream of 100% H$_2$ and 30% H$_2$/70% N$_2$. These

$I_{avg} = 0.21$ A/cm^2, Vcell = 0.74V $I_{avg} = 1.14$ A/cm^2, Vcell = 0.49V

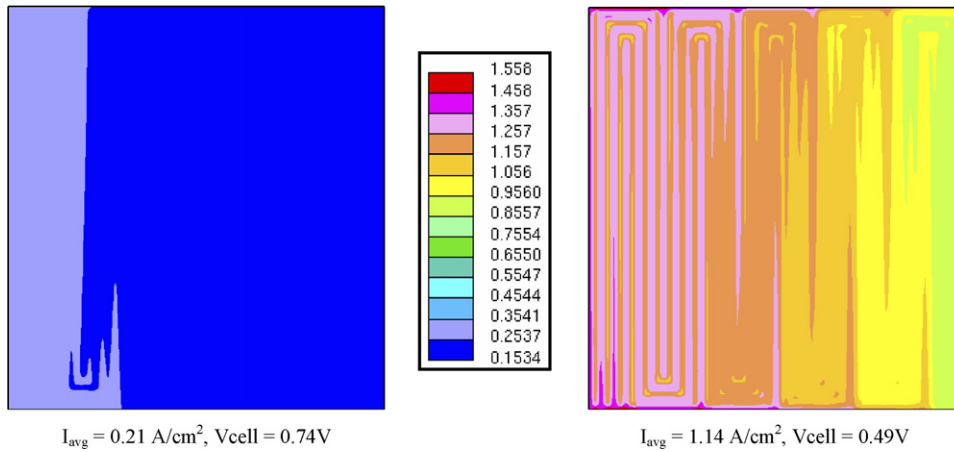Fig. 9. Comparison of local current density (A cm^{-2}) distributions on MEA surface between high and low potentials for condition #1.

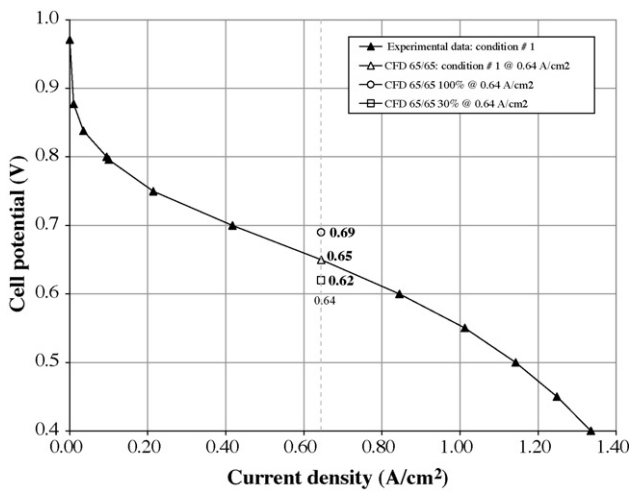Fig. 10. Polarization curves of condition #1 compared to different percentages of hydrogen in nitrogen at $I_{avg} = 0.64$ A cm^{-2}.

results are compared to the numerical solution with 40% H$_2$/60% N$_2$.

Fig. 10 shows the experimental polarization curve of condition #1 with a composition of anode gas stream of 40% H$_2$/60%

N$_2$ compared with the calculated results of 100%, 40%, and 30% hydrogen at 0.64 A cm^{-2}. A hydrogen concentration of 100% gives higher performance (0.69 V) than the same point of experimental condition #1 (0.65 V). For 30% hydrogen in nitrogen, the performance is predicted to be lower (0.62 V) than the experimental data using 40% hydrogen (0.65 V). This is because hydrogen dilution on the anode reduces the partial pressure of hydrogen, thus increasing anode overpotential and dropping its performance.

Fig. 11 shows current density distributions of 100% and 30% hydrogen. The results reveal that the current density distribution with 100% H$_2$ is more uniform than with diluted hydrogen with the highest current density of 0.72 A cm^{-2} at the inlet region and the lowest value of 0.52 A cm^{-2} at the exit region. This uniformity is primarily caused by the uniformity in anode gas composition throughout the cell. The current density distribution for 30% hydrogen is very non-uniform with the highest current density of 0.95 A cm^{-2} at the entrance region to the outlet with the lowest value of almost 0.37 A cm^{-2}. The dilution effect causes a significant reduction of hydrogen toward the outlet resulting in very low current densities.

The local hydrogen mass fraction distribution for 100% hydrogen is very uniform as shown in Fig. 12. The hydrogen
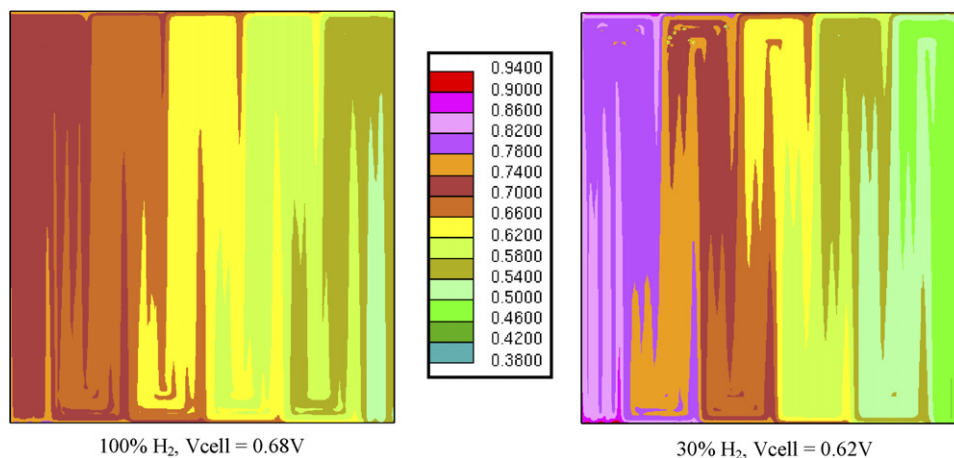

100% H$_2$, Vcell = 0.68V   30% H$_2$, Vcell = 0.62V

Fig. 11. Comparison of local current density (A cm^{-2}) distributions on MEA surface of $I_{avg} = 0.64$ A cm^{-2} between 100% H$_2$ and 30% H$_2$ for condition #1.
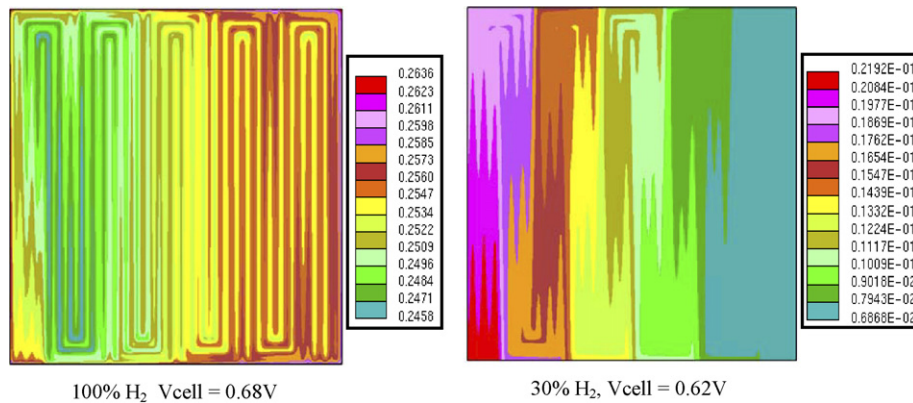
Fig. 12. Comparison of local hydrogen mass fraction distributions on MEA surface of $I_{avg} = 0.64$ A cm^{-2} between 100% H$_2$ and 30% H$_2$ for condition #1.

mass fraction actually increases slightly from inlet toward outlet due to the reduction of water concentration (note that there are only two species at the anode side at this condition, hydrogen and water). For 30% H$_2$, the simulation gives a very non-uniform distribution, which is similar to the current density distribution shown in Fig. 11. The hydrogen mass fraction reduces from inlet toward outlet from a maximum of 0.02 to a minimum of 0.01.

Fig. 13 illustrates the local membrane conductivity for both cases of hydrogen concentration. The distributions are similar to Fig. 5b with the lowest value at the entrance region and highest at the exit region. For 100% hydrogen, the distribution is most uniform and 40% H$_2$ is more uniform than 30% H$_2$. Therefore, the composition of fuel in the anode stream can control the hydration of the membrane thereby affecting the membrane conductivity and its distribution.

4.4. Influence of micro layer

Simulations were performed without the micro diffusion layer for conditions #1 to study the influence of the micro layer on the behavior of the fuel cell. Fig. 14 shows current density and membrane conductivity distributions for condition #1

(65 °C dew point on anode and 65 °C dew point on cathode) without the micro layer. Comparison of Fig. 14a with Fig. 5a, which is the current density distribution including the micro layer reveals that the configuration including the micro layer gives slightly higher performance than the case of no micro layer by 0.02 V at similar averaged current density. The main reason for the higher performance with the micro layer present is indicated by the higher membrane conductivity. Its value including the micro layer (Fig. 5b) is higher throughout the active area of the cell, but particularly in the exit region compared to the case without the micro layer (Fig. 14b). This suggests that the micro layer has a beneficial effect on local water management at this condition, which leads to more water retention in the membrane and, subsequently, a higher membrane conductivity. In addition to this effect, the current density distribution without the micro layer as shown in Fig. 14a shows more non-uniformity than the case including the micro layer (Fig. 5a) with a higher current density at the entrance region and lower values at the exit region. The much lower permeability and diffusivity of the micro layer compared to the macro layer aids in a more even distribution of the reacting gas flows to the MEA surface.
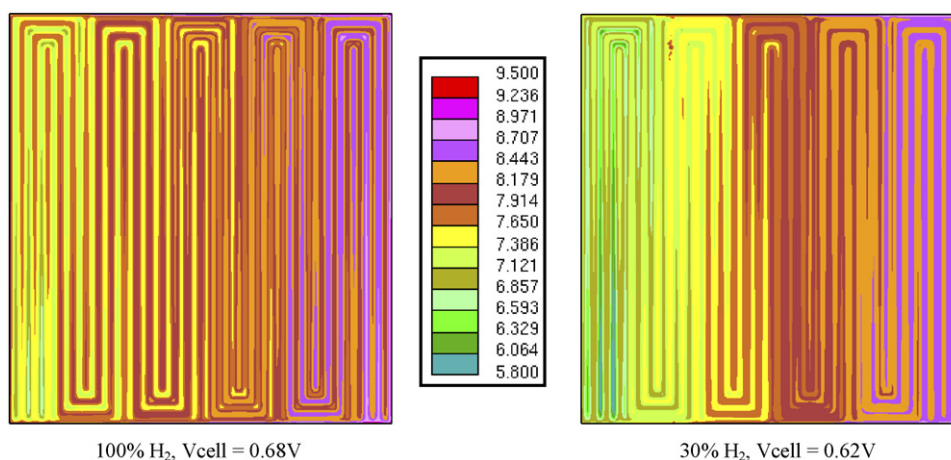

Fig. 13. Comparison of local membrane conductivity (S m^{-1}) distributions on MEA surface of $I_{avg} = 0.64$ A cm^{-2} between neat 100% H$_2$ and 30% H$_2$ for condition #1.
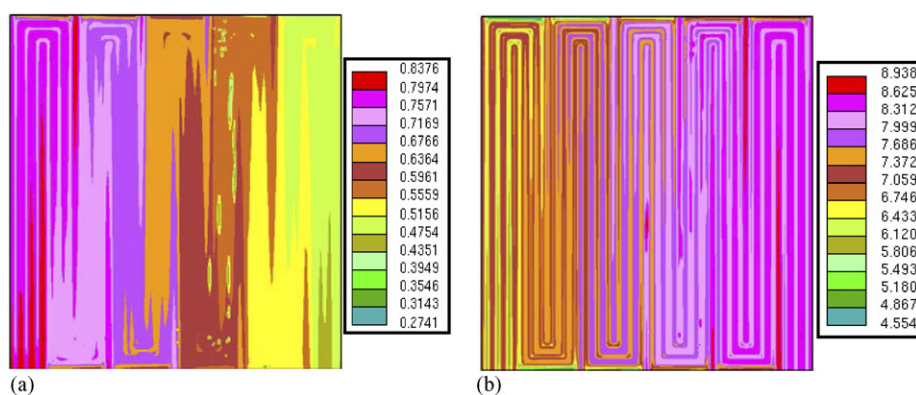
Fig. 14. Local current density (A cm^{-2}) and membrane conductivity distributions at 0.63 V for condition 65 °C/65 °C dew point without micro layer. (a) Current density distribution, $I_{avg} = 0.64$ A cm^{-2}. (b) Membrane conductivity distribution, $\sigma_{avg} = 7.0$ S m^{-1}.

5. Conclusion

Full-cell numerical calculations of PEM fuel cell performance agree very well with experimental data. The cell potentials at four different operating conditions with vastly different humidification conditions are predicted to be within 2% of the experimentally measured value. The simulation provides valuable insight into the local distribution of current density, membrane conductivity, temperature, and transport rates. Comparison of these distributions explains the performance under the different operating conditions. Super-saturation of the incoming gas streams results in a very high current density at the inlet but also to the formation of liquid water (flooding), which lowers the performance due to the increased film resistance for diffusion. Dry gas streams on either anode or cathode cause a low membrane conductivity and low performance. The two cases show opposite current density distributions and reveal details of the water management inside the cell.

This model is able to predict the effect of hydrogen dilution on the cell performance and local distributions. The performance of the cell is decreased by reducing the concentration of hydrogen. This effect not only changes the overall performance but also changes the uniformity of local distributions.

Simulations without the micro porous gas diffusion layer show slightly better performance when the micro layer is present. The local distributions, however, can be very different and it appears that the micro layer assures more uniform local distributions.

References

[1] L.R. Jordan, A.K. Shukla, T. Behrsing, N.R. Avery, B.C. Muddle, M. Forsyth, J. Power Sources 86 (2000) 250.
[2] E. Antolini, R.R. Passos, E.A. Ticianelli, J. Power Sources 109 (2002) 477.
[3] C.Y. Wang, Chem. Rev. 104 (2004) 4727–4766.
[4] J.J. Baschuk, X. Li, J. Power Sources 142 (2004) 134–153.
[5] W-k. Lee, S. Shimpalee, J.W. Van Zee, J. Electrochem. Soc. 150 (2003) A341–A348.
[6] T. Zhou, H. Liu, J. Power Sources 138 (2004) 101–110.
[7] S. Shimpalee, S. Greenway, D. Spuckler, J.W. Van Zee, J. Power Sources 135 (2004) 79–87.
[8] H. Meng, C.Y. Wang, J. Electrochem. Soc. 152 (9) (2005) A1733–A1741.
[9] J.G. Pharoah, J. Power Sources 144 (2005) 77–82.
[10] A.A. Kulikovsky, T. Wüster, A. Egman, D. Stolten, J. Electrochem. Soc. 152 (6) (2005) A1290–A1300.
[11] W. Ying, Y.-J. Sohn, W.-Y. Lee, J. Ke, C.-S. Kim, J. Power Sources 145 (2005) 563–571.
[12] B.R. Sivertsen, N. Djilali, J. Power Sources 141 (2005) 65–78.
[13] P.H. Oosthuizen, L. Sun, K.B. McAuley, Appl. Therm. Eng. 25 (2005) 1083–1096.
[14] H. Meng, C.Y. Wang, J. Fuel Cells 5 (4) (2005) 455–462.
[15] S. Litster, J.G. Pharoah, G. McLean, N. Djilali, J. Power Sources 156 (2) (2006) 334–344.
[16] P.P. Mukherjee, C.Y. Wang, J. Electrochem. Soc. 153 (5) (2006) A840–A849.
[17] X.L. Liu, W.Q. Tao, Z.Y. Li, Y.L. He, J. Power Sources 158 (1) (2006) 25–35.
[18] Star-CD 3.2 Methodology, CD Adapco Group, http://www.adapco.com.
[19] ES-PEMFC Methodology and Tutorial Manual, CD Adapco Group, http://www.adapco.com.